Nonplanar Fault Source Modeling of the 2008 Mw6.9 Iwate-Miyagi Inland Earthquake in Northeast Japan

Takahiro Abe[1], Masato Furuya[1#] and Youichiro Takada[2]

1. *Department of Natural History Sciences, Hokkaido University, N10W8, Kita-ku, Sapporo, Hokkaido, 060-0810, Japan*

2. *Kamitakara Observatory, Disaster Prevention Research Institute, Kyoto University, 2296-2 Hongo, Kamitakara, Takayama, Gifu 506-1317, Japan*

Corresponding author: furuya@mail.sci.hokudai.ac.jp

Abstract

We use crustal deformation data sets acquired by the Phased Array type L-band Synthetic Aperture Radar (PALSAR) and the Japanese nationwide GPS network (GEONET) to develop a fault source model for the 2008 Iwate-Miyagi Inland earthquake (Mw 6.9) which occurred on June 14 2008 in the northeastern Honshu, Japan. The PALSAR data include interferometric SAR (InSAR), range offset, and azimuth offset acquired from both ascending and descending paths. The range and azimuth offset data are the only quantitative deformation signals around the epicenter, and exhibit complicated signals that were not detected by the GPS data. We refine our preliminary model with the use of Green's functions from triangular dislocation elements to represent non-planar fault geometries. Whereas a single segment model can well explain the GPS data, it generates significant misfit residuals in the offset data, and thus both west-dipping and east-dipping segments are necessary, as also suggested from aftershock distribution data. The moment magnitude of the west-dipping and east-dipping faults is 6.53 and 6.76, respectively, and the total sum, 6.87, is almost identical to the seismological moment magnitude. This result suggests that both segments contributed equally to the total seismic moment, demonstrating a complex rupture process of the inland earthquake.

Introduction

The Iwate-Miyagi inland earthquake with a moment magnitude (Mw) 6.9 occurred on June 14 2008 in the northeastern Honshu, Japan (Fig. 1). The epicenter is located along the Ou Backbone Mountains, which developed as consequences of island-arc volcanisms as well as intra-plate earthquakes like the earthquake we study here. Meanwhile, continuous GPS observations have indicated strain concentration zones along the Ou Backbone Mountains, and high seismicity is known with hypocenters distributed at depths shallower than 15 km (e.g., Miura *et al.*, 2004). Thus, the reverse faulting earthquake with a roughly east-west compression axis is not surprising. Nevertheless, the earthquake at the location was unexpected, because there were no previously known active faults near the epicenter. While the earthquake consequently confirmed a difficulty to perform accurate hazard assessments for inland earthquakes (England and Jackson, 2011), we should note that our understandings on the generation mechanisms of inland earthquakes are still very limited due to the lack of detailed observation data.

Although a variety of crustal deformation observations for the earthquake have been reported, a comprehensive fault source model for the co-seismic deformation has yet to be proposed, primarily because both the observed crustal deformation and aftershock distribution

1 are highly complicated. For example, based on the complex spatial distribution of SAR-based
2 co-seismic deformation data, Takada *et al.* (2009) proposed a fault model that consists of one
3 east-dipping and four west-dipping rectangular segments. Detailed aftershock distribution
4 data also support the existence of both east-dipping and west-dipping faults (Takada *et al.*,
5 2009; Okada *et al.*, 2012), but each of the fault segments by Takada et al's model consists of a
6 uniform slip without distributed slips. Ohta *et al.* (2008) inferred two west-dipping faults with
7 distributed slips to account for the GPS data. Near the epicenter, however, there are few GPS
8 observation points, and as we confirm below it is difficult to explain the detailed signals
9 revealed by SAR data only with a west-dipping fault segment. Moreover, while many
10 previous studies assumed rectangular-planar fault models, the spatial distributions of the
11 detected crustal deformation data are highly complicated so that the use of rectangular planar
12 fault element would inevitably lead to physically unrealistic overlaps and/or gaps of fault
13 segments (e.g., Maerten *et al.*, 2005).
14 In order to explain the observed data without the aforementioned geometric inconsistencies,
15 it is necessary to assume non-planar fault surfaces. While it has long been recognized from
16 geological observations, it should be noted that only after the advent of SAR-based crustal
17 deformation data did we begin to recognize the importance of using non-planar fault elements

and their corresponding dislocation Green's functions (Maerten *et al.*, 2005; Furuya and Yasuda, 2011). Developing a realistic fault model in terms of its geometry, we can better understand the generation mechanisms of any individual earthquakes and further advance our knowledge on the complexities of earthquakes in general. Realistic co-seismic fault models are also important for a proper interpretation of post-seismic deformation signals.

In this paper, we refine Takada *et al*'s preliminary fault model and develop a non-planar fault slip distribution model for the 2008 Iwate-Miyagi inland earthquake, so that we can reasonably explain all the available data such as SAR, GPS and aftershock distribution data sets. Based on the derived fault model and a comparison to Bouguer gravity anomaly data, we also discuss the geological background of the 2008 Iwate-Miyagi inland earthquake. We point out that the location of the inferred east-dipping fault closely matches to a steep gradient of Bouguer gravity anomaly, which may have an implication for hazard assessments of inland earthquakes in NE Honshu.

SAR Data processing

We processed L-band (wavelength 23.6 cm) Synthetic Aperture Radar (SAR) data acquired by ALOS/PALSAR (Advanced Land Observing Satellite/Phased Array-type L-band SAR) that

was launched by the Japan Aerospace Exploration Agency in 2006; its operation terminated in April 2011. We used the Gamma software to process from their level 1.0 data (Wegmüller and Werner, 1997). Figure 1 shows the observed areas, and the solid and dashed rectangles indicate the ascending and descending path, respectively. The dash-dot rectangle indicates our modeling area. Details of our analyzed SAR data are listed in Table 1.

Our SAR data processing procedures are the same as in previous studies (Kobayashi *et al.*, 2009; Furuya *et al.*, 2010*;* Furuya and Yasuda, 2011), in which we applied both InSAR and pixel-offset techniques. InSAR data are derived from the phase differences of two temporally separated SAR images, and have high sensitivity to ground displacements with an accuracy on the order of 2-3 cm. Also, because the L-band microwaves in PALSAR can penetrate through vegetations, interferometric coherence is not seriously lost even in mountainous areas, where few continuous GPS stations are available. However, even after the removal of orbital and topographic phases, the InSAR data include artifacts originating in the troposphere, ionosphere and from errors of the satellite orbit data. In this study, topography-correlated tropospheric artifacts were removed with the aid of a digital elevation model, and the long-wavelength residual phases were removed by fitting them with second-order polynomials. In the case of the studied earthquake, we could not unwrap the InSAR phase

data around the epicenter, because the spatial gradient of the ground displacements were extremely large. Those signals are, however, the most critical data to derive a fault source model. In order to fill the gaps in InSAR data, we performed pixel-offset technique to the intensity data of the same SAR images instead of using phase differences (Strozzi *et al.*, 2002). In this technique, we divide one single-look complex (SLC) image into a number of patches and derive their offsets from the corresponding patches in the other SLC image with a precision of sub-pixel level, by cross-correlating backscatter intensity samples from a master image (the data before earthquake) with those from a slave image (the data after earthquake); the accuracy of pixel-offset technique is on the order of 10-20 cm for ALOS data with ~300 m pixel (Kobayashi *et al.*, 2009). The derived offset is composed of two components, which consist of displacements along the radar line of sight (LOS, range offset) and those along the satellite orbit track (azimuth offset).

This earthquake took place in mountainous areas, where elevation differences could cause large artifacts in the pixel offsets due to a slight difference in satellite positions before and after the earthquake (stereoscopic effect) (Michel *et al.*, 1999; Kobayashi *et al*., 2009). We removed this artifact by elevation-dependent co-registration fully incorporating the 10 m mesh digital elevation map provided by the Geospatial Information Authority of Japan.

Observation Results

Figures 2 show the observed ground displacement data acquired by InSAR and pixel-offset technique, respectively. Figures 2a and 2b are the wrapped InSAR data, which are unwrapped as in Figures 2c and 2d. The unwrapped InSAR data in Figures 2c and 2d indicate that the displacement amplitude is greater than 1 m along the radar LOS even outside the incoherent epicenter areas, and the observed deformation signals are overall consistent with those expected from reverse faulting by WNW-ESE compression. InSAR data alone, however, cannot tell if the actual source fault(s) are dipping to the west, east or both, because the phase data around the epicenter areas could not be unwrapped. Therefore, pixel-offset data play a complementary and important role to reveal detailed displacement images around the epicenter. This is particularly the case in the 2008 Iwate-Miyagi Inland earthquake, because the epicenter areas are located in densely vegetated mountains, and field-based surface fault mapping is virtually impossible; the correspondence of offset data to surface faulting has been confirmed, for instance, in the 2008 Wenchuan earthquake (Koyabashi *et al*. 2009; Furuya *et al*. 2010). Whereas the range-offset data could be used to help phase unwrapping (Yun *et al*. 2007), we directly employed the offset data to perform fault source modeling. Figures 2e-2h

illustrate that the displacements are not only large in amplitude but also distributed in a spatially complex fashion. The azimuth offset data in Figure 2g show streaks due to the ionospheric disturbances (Meyer *et al*., 2006; Kobayashi *et al*., 2009); we did not use the azimuth offset data in Figure 2g for the fault source modeling. As pointed out in Takada *et al.* (2009), the range offset data in Figures 2e and 2f reveal remarkable jumps not only to the east of the epicenter but also around the eastern edge of Mt. Kurikoma, which cannot be explained by a west-dipping fault alone. Moreover, these jumps strongly suggest that there is not a single straight fault trace but multiple and curved fault traces on the surface. Furthermore, the azimuth offset data from the descending orbit in Figure 2h show sign changes across the jumps around the GPS station, Kurikoma2, suggesting that the slip direction is reversed around the jump because the azimuth offset is most sensitive to the north-south motion. We interpret these discontinuities in the pixel-offset data as caused by not only west-dipping segment but also east-dipping one (Takada *et al*. 2009).

In Figures 3, we show GPS-based horizontal and vertical displacements (black arrows) together with the aftershock distribution; the GPS displacements and aftershock distribution data are provided from the Geospatial Information Authority of Japan and the Group for the aftershock observations of the Iwate-Miyagi Inland Earthquake, respectively. The GPS

displacement data clearly indicate east-west convergence (Fig. 3a), and are overall consistent with those expected from reverse faulting. The ground displacements at the station, Kurikoma2, located to the southeast of Mt. Kurikoma are remarkably large, moving ~150 cm southeastward horizontally and ~200 cm upward.

Modeling Results -From Single Segment to Double Segments-

Given the spatially complex distributions in the ground displacements revealed by the pixel-offset data, we develop a non-planar fault model that can consistently account for both InSAR, pixel-offset, and GPS data, assuming slip distribution on curved fault planes in a homogeneous elastic half space. Although Okada's analytical solutions are useful to express ground displacements due to dislocation sources in a homogeneous elastic half space (Okada, 1992), they assume a rectangular dislocation element, and thus will generate mechanically incompatible gaps and/or overlaps if they are used to represent non-planar fault source geometries (Maerten *et al*., 2005; Furuya and Yasuda, 2011). To compute the ground displacements from a non-planar fault model, we employ analytical solutions due to dislocation sources on triangular dislocation elements (Meade, 2007).

The horizontal location of the top edge of the faults was visually inspected from the

pixel-offset data, and the bottom depth of the faults was fixed to be 10 km in reference to the aftershock distribution. The depth of the top edge of the faults was fixed to be 0.5 km. In order to generate triangular mesh coordinates for the non-planar fault, we use a mesh-generation software, Gmsh (Geuzaine and Remacle, 2009). We first give 3D coordinates of several control points on each fault segment. Those points are interpolated with splines to form each non-planar fault surface. To avoid unnecessarily complicated fault geometry, the bottom edge was set as straight as possible. Because the resolving power of slip distribution becomes worse at deeper depth (Bos and Spakman, 2003), we made the mesh size smaller (larger) at shallower (deeper) depth; the characteristic lengths were set 1.0 km (4.0 km) at shallowest (deepest) control points. The Gmsh automatically generates 3D mesh coordinates at all the nodes, with which we can compute the dislocation Green's function from each triangular slip patch. Then, it is straightforward to invert for the slip distribution as a linear least-squares problem (e.g., Jónsson *et al*., 2002; Simons *et al*., 2002; Wright *et al*., 2003). We also performed the quad-tree decomposition technique to reduce the number of data (e.g., Jónsson *et al*., 2002; Lohman and Simons, 2005). In deriving slip distribution, we applied both a smoothness constraint with the scale-dependent umbrella operator (Maerten *et al*., 2005) and a non-negativity constraint on the signs of fault slip, in which only left lateral

and reverse-fault slip components were allowed for the solution.

We first developed a single-segment non-planar fault model that explains the GPS data alone. Shown in Figures 3 are the calculated GPS-displacements (while arrows) based on a single-segment slip distribution model in Figure 4. We derived the fault location and geometry with a trial-and-error approach. The single segment fault model in Figures 4 may be regarded as a non-planar version of the previous GPS-based model (Ohta *et al*., 2008). Figures 4 show the dip- and strike slip distribution on the fault surface. The maximum dip slip is ~5 m and that of strike slip is nearly 0.5 m. These slip distributions are consistent with a reverse fault motion and the Global CMT solution. This model can well explain the GPS displacements without setting an east-dipping fault segment. As shown below, however, the single-segment slip distribution model fails to account for the SAR-based displacement data.

Using the fault geometry and slip parameters in Figure 4, we examined whether or not the single-segment fault model could explain the SAR data. Figures 5 and 6 show the calculated data and misfit residuals. The calculated InSAR data in Figures 5a and 5c generate misfit residuals in Figures 5b and 5d greater than 50 cm in radar LOS above the largest slip patches in Figures 4. Moreover, the calculated range-offset data in Figures 6a and 6c reveal notable discontinuities in the misfit residuals in Figures 6b and 6d. These results suggest that the

SAR-based displacements are not simple enough to be explained by the GPS-based fault model, and that the GPS data coverage is not dense enough in the mountain areas.

Besides the pixel-offset data around the epicenter, the aftershock distribution data also support an east-dipping fault segment. Figures 7 show the aftershock distributions and their cross sections from the north to the south. While the upper-right panel in Figure 7 obviously suggests a west-dipping fault segment, and there appear few evidences for east-dipping segment to the north, the middle- and lower-right panels in Figure 7 indicate lineaments that suggest an east-dipping fault segment, whose locations closely match the jumps in the range offset data in Figures 2e and 2f.

Figures 8, 9, and 10 illustrate the calculated and misfit residuals of GPS, InSAR, and pixel-offset data, respectively, based on our preferred two-segment non-planar fault slip distribution model in Figure 11. A plan view of the source model location is also illustrated in Figures 8, 9, and 10. Because the bottom depth of both west-dipping and east-dipping segments is fixed to be 10 km, the two non-planar surfaces are crossing at a depth around 5 km (Figures 11e and 11f). While the crossing at depth appears mechanically incompatible at first glance, we note that the inferred slip amplitude in the east-dipping segment is quite small at deeper depth. We again derived the model geometry and slip distributions in Figure 11 by

trial-and-error. In solving for the slip distribution, we use InSAR and range offset data along the two tracks, one azimuth offset at the descending track and the GPS data. We normalized each data set with weights of 5 cm, 20 cm, 25 cm and 1 cm and 5 cm for InSAR, range-offset, azimuth-offset, horizontal GPS and vertical GPS data, respectively.

Figures 8 indicate that the observed and calculated GPS displacements are overall in good agreement as already shown in Figures 3 based on a simpler fault model in Figures 4. However, we should note that the observed GPS displacements data are explained quite differently between Figures 3 and 8. Whereas the displacements at the Kurikoma2 station are explained by the ~5 m dip slip in the west-dipping fault in Figure 3, they are mostly explained by the ~3 m slip in the east-dipping fault in Figure 8. While these results demonstrate a non-uniqueness of fault source modeling of geodetic displacement data, we believe that the fault model in Figure 11 is more realistic, because it is consistent not only with the GPS data but also with other data sets.

Figures 9 and 10 show the calculated and misfit residuals of the InSAR data and pixel-offset data, respectively. Compared with the results in Figures 5 and 6, the misfit residuals are reduced significantly in both InSAR and pixel-offset data. Due to the east-dipping fault, the calculated data become more consistent with the observed data,

particularly in the range-offset data (Figs. 10a-10d).

Figures 11 show the dip and strike slip distribution on the fault surface of our two-segment model. Figures 11a and 11b indicate the dip slip distributions for the east-dipping and west-dipping segment, respectively. While the dip slip component distributed broadly in the west-dipping segment (Fig. 11b), it is rather localized in the southern part of the east-dipping segment, and little dip slip is derived in the northern part (Figs. 11a and 11c). The inferred slip distributions are consistent with the lack of east-dipping lineament in the aftershock distribution in Figure 6. The moment magnitude inferred from the east-dipping and west-dipping fault is 6.76 and 6.53, respectively, with a total of 6.87, which is consistent with the Global CMT solution; the rigidity is assumed to be 30 GPa. Therefore, it is likely that the earthquake rupture occurred nearly simultaneously on the two fault segments.

Figures 12 are our estimated one-sigma uncertainties in the inferred slip distribution in Figures 11, which were derived by perturbing the calculated signals from the estimated slip distribution with synthetic 2D correlated noise and repeating the linear inversion 200 times (Wright *et al*., 2003; Furuya *et al*., 2010; Furuya and Yasuda, 2011). Here we did not apply non-negativity constraint to the slip directions. The uncertainty estimates indicate that the slip magnitude at shallower depth was reliably estimated, but those at deeper depths have

uncertainties on the order of 10-30 cm or more.

Because both range and azimuth offset data are available from two different orbit tracks, we can generate 3D displacement fields (e.g., Fialko *et al*., 2001; Funning *et al*., 2005). Figure 13a shows the observed 3D displacements derived by Ando and Okuyama (2010), which are based on virtually the same SAR data sources as we used in deriving the fault model. Figures 13b and 13c are the calculated 3D displacements from the source model in Figure 11 and the misfit residuals, respectively. Including the east-dipping fault, the observed 3D displacements could be overall well reproduced in the calculated ones. However, there remain large misfit residuals particularly near the top edge of the west-dipping fault to the southeast (Figure 13c), which was also clear in the range-offset data along the descending track 57 (Figure 10d). Comparing Figure 13a with 13b around the large residuals, we realize that the displacements amplitudes in the observed one are much smaller than those in the calculated one in both horizontal and vertical components. Namely, the contribution of the west-dipping fault to the total displacement fields could be smaller than we have modeled. Although the residuals in Figure 13c may suggest even more complex fault geometry for the west-dipping fault to the east, we stopped our trial-and-errors for optimization, because our main target was to refine a source model for the east-dipping segment and there were fewer observational constraints

around the west-dipping fault. Moreover, Figure 13a indicates highly heterogeneous distribution of displacements even outside the clear steps in the vertical displacements, which are unlikely to be explained by deformation response of dislocation sources inside a homogeneous elastic body, and could be non-elastic deformation signals (e.g., landslide) triggered by the earthquake.

Discussion

Geological Origin of the 2008 Iwate-Miyagi inland earthquake

Major differences of our fault model in Figure 11 from Takada *et al*'s preliminary model are not only the use of a triangular dislocation element to represent non-planer fault surfaces but also the north-south extension of the east-dipping segment. With this extension, particularly toward the south, we were able to reduce the misfit residuals significantly in pixel-offset data, and were also able to account for the enigmatic GPS displacements at the Kurikoma2 station. Why did the earthquake faults exhibit such a complex geometry? We speculate on the geological origin, comparing the faults' location with the Bouguer gravity anomaly data from Geological Survey of Japan (2004). Figure 14 illustrates a Bouguer anomaly with an assumed density of 2.3 g/cm^3 as well as the top edges of our two-segment

fault model. We observe that the significantly deformed area by the 2008 Iwate-Miyagi Inland earthquake largely corresponds to the high Bouguer anomaly area, which is surrounded by low anomaly areas to the east and west. In particular, it should be noted that the steep gradient in the gravity anomaly along the western edge of the gravity high area locates close to the top edges of the east-dipping fault of our model. In fact, geologists have reported that the low anomalies located to the west and south of Mt. Kurikoma (Fig.14), characterized by their round shape, correspond to the late Cenozoic collapse calderas (e.g., Yoshida *et al.*, 2001; Nunohara *et al*., 2010). Considering those geological reports, we may conclude that the east-dipping fault has been affected by the existence of the caldera rims. We interpret that the caldera wall acted as a rupture surface, and that many hidden ruptures associated with the formation of collapse calderas could be the origin of the complex fault geometry. The 1996 Onikobe earthquakes occurred ~15 km to the SE of Mt. Kurikoma also generated complicated crustal deformation signals, which were interpreted in association with the old caldera structures (Takada and Furuya, 2010). Overall, the crustal heterogeneity due to the dense distribution of the old calderas appears to make surface deformation so complicated. Hence, although our fault model is more complicated than Takada *et al*'s preliminary model, there still remain misfit residuals in the observed geodetic data.

Pros and cons of triangular dislocation element

There are advantages and disadvantages of triangular dislocation elements over rectangular dislocation elements. While triangular dislocation elements can be used to represent arbitrarily complex faults, unless there are firm observational constraints around the hypocenter region (e.g., aftershocks, pixel-offset data), it is difficult to optimize the fault geometry because the degrees of freedom in the parameter settings are much greater than those in case of rectangular elements. Whereas we derived the source model by trial-and-errors, it is an important future work to develop an efficient approach to optimize the locations and geometry of non-planar fault model based on triangular dislocation elements.

Seismological studies on the fault source model

Suzuki *et al* (2010) inferred a distributed slip model on a west-dipping single fault plane, inverting for the velocity waveform data derived from the regional strong motion network. However, in order to account for not only the static displacements but also a temporal evolution of a tilt record near the epicenter, Fukuyama (2009) concluded that conjugate faults should have ruptured simultaneously to main rupture; the tilt data record was derived from the same regional strong motion data. This is consistent with our finding of roughly equal contribution of the east-dipping and west-dipping fault segments to the total seismic moment.

Conclusion

Using SAR- and GPS-based co-seismic deformation data sets, we derived a non-planar fault source model for the 2008 Iwate-Miyagi Inland earthquake (Mw 6.9), NE Japan. Although a single-segment fault model can well explain the GPS data, there arise significant misfit residuals if it is applied to the SAR data. We propose a two-segment fault model consisting of east-dipping and west-dipping fault planes, which are consistent with independently observed aftershock distributions as well as the Bouguer gravity anomalies.

Data and Resources

We generated all the interferograms and pixel-offset data from PALSAR level 1.0 data, using the commercial software package from Gamma Remote Sensing. PALSAR level 1.0 data used in this study were provided from the PALSAR Interferometry Consortium to Study our Evolving Land surface (PIXEL) under a cooperative research contract with Japan Aerospace Exploration Agency (JAXA). The ownership of PALSAR data belongs to the Ministry of Economy, Trade and Industry (METI) and JAXA. PALSAR level 1.0 data are also available from the Remote Sensing and Technology Center of Japan, http://www.alos-restec.jp (last

accessed April 2012). GPS data were released from the Geospatial Information Authority of Japan. The aftershock data were given from the Group for the aftershock observations of the Iwate-Miyagi Inland Earthquake in 2008. The Global Centroid Moment Tensor Project database was searched using www.globalcmt.org/CMTsearch.html (last accessed April 2012). All figures in this paper were made using Matlab (http://www.mathworks.com).

Acknowledgements

The observed SAR-based 3D displacement data were given by Dr. Satoshi Okuyama. We also thank Dr. Takeyoshi Yoshida for discussing the geological origin of the complex fault geometries. We acknowledge Dr. Tim Wright and an anonymous reviewer for their constructive comments that significantly improved the original manuscript.

References

Ando, R., and S. Okuyama (2010), Deep roots of upper plate faults and earthquake generation illuminated by volcanism, *Geophys. Res. Lett*., **37**, L10308, doi 10.1029/2010GL042956.

Bos, A. G., and W. Spakman (2003). The resolving power of coseismic surface displacement data for fault slip distribution at depth, *Geophys. Res. Lett*., **30**, no. 21, 2110, doi

10.1029/2003GL017946.

England, P., and J. Jackson (2011), Uncharted seismic risk, *Nature Geosci*., **4**, 348-349, doi 10.1038/ngeo1168.

Fukuyama, E. (2009), A Possible Coseismic Rupture on Conjugate Faults, *Eos Trans. AGU*, **90**(52), Fall Meet. Suppl., Abstract S33C-03

Fialko, Y., M. Simons, and D. Agnew (2001), The complete (3-D) surface displacement field in the epicentral area of the 1999 MW 7.1 Hector Mine Earthquake, California, from space geodetic observations, *Geophys. Res. Lett*., **28**(16), 3063-3066.

Funning, G. J., B. Parsons, T. J. Wright, J. A. Jackson, and E. J. Fielding (2005), Surface displacements and source parameters of the 2003 Bam (Iran) earthquake from Envisat advanced synthetic aperture radar imagery, *J. Geophys. Res.*, **110**, B09406, doi:10.1029/2004JB003338.

Furuya, M., T. Kobayashi, Y. Takada, and M. Murakami (2010). Fault Source Modeling of the 2008 Wenchuan Earthquake Based on ALOS/PALSAR Data, *Bull. Seismol. Soc. America*, **100**, no. 5B, 2750-2766, doi 10.1785/0120090242.

Furuya, M., and T. Yasuda (2011). The 2008 Yutian normal faulting earthquake (Mw 7.1), NW Tibet: Non-planar fault modeling and implications for the Karakax Fault,

Tectonophys., **511**, 125-133, doi 10.1016/j.tecto.2011.09.003.

Geological Survey of Japan (2004). Gravity CD-ROM of Japan. Ver. 2, Geological Survey of Japan. AIST.

Geuzaine, C., and J.F. Remacle (2009). Gmsh: a three-dimensional finite element mesh generator with built-in pre- and post-processing facilities, Int. *J. Num. Meth. Eng*., **79**, no 11, 1309–1331.

Jónsson, S., H. Zebker, P. Segall, and F. Amelung (2002). Fault Slip Distribution of the 1999 Mw 7.1 Hector Mine, California, Earthquake, Estimated from Satellite Radar and GPS Measurements, *Bull. Seismol. Soc. America*, **92**, no.4, 1377-1389.

Kobayashi, T., Y. Takada, M. Furuya, and M. Murakami (2009). Locations and types of ruptures involved in the 2008 Sichuan earthquake inferred from SAR image matching, *Geophys. Res. Lett*., **36**, L07302, doi 10.1029/2008GL036907.

Lohman, R. B., and M. Simons (2005). Some thoughts on the use of InSAR data to constrain models of surface deformation: Noise structure and data downsampling, G^3, **6**, Q01007, doi 10.1029/2004GC000841.

Maerten, F., P. Resor, D. Pollard, and L. Maerten (2005). Inverting for Slip on Three-Dimensional Fault Surfaces Using Angular Dislocations, *Bull. Seismol. Soc.*

America, **95**, no. 5, 1654-1665, doi 10.1785/0120030181.

Meade, B. J.（2007）. Algorithms for the calculation of exact displacements, strain, and stresses for triangular dislocation element in a uniform elastic half space, *Comp. Geosci*., **33**, 1064-1075, doi 0.1016/j.cageo.2006.12.003.

Meyer, F., R. Bamler, N. Jakowski, and T. Fritz (2006). Methods for small scale ionospheric TEC mapping from broadband L-band SAR data, in *Proc. IGARSS*, Denver, CO, Jul. 31-Aug. 4., 3735-3738.

Michel, R., J.-P. Avouac, J. Taboury (1999). Measuring ground displacements from SAR amplitude images: Application to the Landers earthquake, *Geophys. Res. Lett*., **26**, 875–878.

Miura, S., T. Sato, A. Hasegawa, Y. Suwa, K. Tachibana, and S. Yui (2004). Strain concentration zone along the volcanic front derived by GPS observations in NE Japan arc, *Earth Planets Space*, **56**, no 12, 1347-1355.

Nunohara, K., T. Yoshida, R. Yamada, S. Maeda, K. Ikeda, Y. Nagahashi, A. Yamamoto, and T. Kudo (2010). Geology and geologic structure around the area of hypocenter of the 2008 Iwate-Miyagi Nairiku earthquake (in Japanese), *Monthly Earth*, **32**, 356-366.

Ohta, Y., M. Ohzono, S. Miura, T. Iinuma, K. Tachibana, K. Takatsuka, K. Miyano, T. Sato,

and N. Umino (2008). Coseismic fault model of the 2008 Iwate-Miyagi Nairiku earthquake deduced by a dense GPS network, *Earth Planets Space*, **60**, no 12, 1197-1201.

Okada, T, N. Umino, A. Hasegawa, and Group for the aftershock observations of the Iwate-Miyagi Nairiku Earthquake in 2008 (2012). Hypocenter distribution and heterogeneous seismic velocity structure in and around the focal area of the 2008 Iwate-Miyagi Nairiku Earthquake, NE Japan: Possible seismological evidence for a fluid driven compressional inversion earthquake, *Earth, Planets and Space*, in press.

Okada, Y. (1992). Internal deformation due to shear and tensile faults in a half-space, *Bull. Seismol. Soc. Am.* **82**, 1018–1040

Simons, M., Y. Fialko, and L. Rivera (2002). Coseismic Deformation from the 1999 Mw 7.1 Hector Mine, California, Earthquake as Inferred from InSAR and GPS Observations. *Bull. Seismol. Soc. Am.* **92**, no 4. 1390–1402, doi 10.1785/0120000933.

Strozzi, T., A. Luckman, and T. Murray (2002). Glacier motion estimation using satellite radar offset-tracking procedures, *IEEE Trans. Geosci. Remote Sens*., **40** (11), 2384-2391.

Suzuki, W., S. Aoi, and H. Sekiguchi (2010), Rupture Process of the 2008 Iwate-Miyagi Nairiku, Japan, Earthquake Derived from Near-Source Strong-Motion Records, *Bull. Seismol. Soc. America*, **100**, no. 2, 256-266, doi 10.1785/0120090043.

Takada, Y., T. Kobayashi, M. Furuya, and M. Murakami (2009). Coseismic displacement due to the 2008 Iwate-Miyagi Nairiku earthquake detected by ALOS/PALSAR : preliminary results, *Earth Planets Space*, **61**, no 4. e9-e12.

Takada, Y., and M. Furuya (2010). Aseismic slip during the 1996 earthquake swarm in and around the Onikobe geothermal area, NE Japan, *Earth Planet. Sci. Lett.*, **290**, 302-310, doi 10.1016/j.epsl.2009.12.024.

Wegmüller, U., and C. L. Werner (1997). Gamma SAR processor and interferometry software, In *Proc. of the 3rd ERS Symposium*, European Space Agency Spec. Publ., ESA SP-414, 1686–1692.

Wright, T. J., Z. Lu, and C. Wicks (2003). Source model of the M_w 6.7, 23 October 2002, Nenana Mountain earthquake (Alaska) from InSAR, *Geophys. Res. Lett*. **30**, 1974, doi 10.1029/2003GL01827.

Yoshida, T., (2001). The evolution of arc magmatism in the NE Honshu arc, Japan, Sci. Rep. Tohoku Univ., **36**, 131-149.

Yun, S.-H., H. Zebker, P. Segall, A. Hooper, and M. Poland (2007). Interferogram formation in the presence of complex and large deformation, *Geophys. Res. Lett.*, **34**, L12305, doi 10.1029/2007GL029745.

Table 1 Data lists used in this study

Orbit[$]	Path	Frame	Dates	Bperp[#] (m)
A	402	760-770	2007/06/21-2008/06/23	-303
D	57	2830-2840	2007/08/29-2008/07/16	-774

Captions for Table and Figures

Table 1: $: A and D stand for ascending and descending orbit, respectively. #: Bperp stands for the perpendicular baseline component, and is derived by projecting the baseline (spatial separation of repeating orbits) onto the direction perpendicular to the radar line-of-sight.

Figure 1: (a) Studied area of the Iwate-Miyagi Inland Earthquake and nearby cities, and the observed areas by ALOS/PALSAR (solid and dashed boxes). Solid and dash boxes represent ascending and descending orbit, respectively. (b) Expanded area of the dash-dot box in Figure 1a. Locations of major mountains and GPS stations near the epicenter are shown. Solid box indicates the area in Figure 2.

Figure 2: Observed deformation data acquired by ALOS/PALSAR. (a, b) Wrapped InSAR

phase data derived from ascending track #402 and descending track #57, respectively. (c, d) Unwrapped InSAR data derived from ascending track #402 and descending track #57, respectively. (e, f) Range component of pixel-offset tracking data derived from ascending track #402 and descending track #57, respectively. (g, h) Azimuth component of pixel-offset tracking data derived from ascending track #402 and descending track #57, respectively. The star and triangle depict the epicenter and Mt. Kurikoma, respectively. The solid dot indicates the location of the GEONET GPS site, Kurikoma2.

Figure 3: Observed (black) and calculated (white) GPS displacement vectors for horizontal (left panel) and vertical (right panel) component, respectively. The scale-bar for the vertical displacement at the site, Kurikoma2, is an order-of-magnitude greater than the others. The calculated GPS displacements are based on a west-dipping fault model with distributed slip as shown in Figure 4. Plan view of the fault model in Figure 4 is also indicated with black with thick line representing the top edge. The star and triangle indicate the epicenter and Mt. Kurikoma, respectively.

Figure 4: Geometry and slip distribution of a west-dipping fault model inferred from GPS

data alone. (a) Dip slip component, (b) Left-lateral slip component. Note the difference in the scale of color bars.

Figure 5: (a) Calculated InSAR data for the ascending track 402 from the fault model in Figure 4, and (b) misfit residuals from the observed one in Figure 2c. (c) Calculated InSAR data for the descending track 57 from the fault model in Figure 4, and (d) misfit residuals from the observed one in Figure 2d.

Figure 6: (a) Calculated range offset data for the ascending track 402 from the fault model in Figure 4, and (b) misfit residuals from the observed one in Figure 2e. (c) Calculated range offset data for the descending track 57 from the fault model in Figure 4, and (d) misfit residuals from the observed one in Figure 2f. (e) Calculated azimuth offset data for the descending track 57 from the fault model in Figure 4, and (f) misfit residuals from the observed one in Figure 2h.

Figure 7: (Left) Plan view of the aftershocks, and (Right) their three cross-sections from the north to the south. The white lines indicate the location of the two-segment model inferred

from GPS and SAR data; the geometry and slip distribution are shown in Figure 11. The thick lines indicate the top edge of our fault model. The star and triangle indicate the epicenter and Mt. Kurikoma, respectively.

Figure 8: Observed (black) and calculated (white) GPS displacement vectors for horizontal (left panel) and vertical (right panel) component, respectively. The scale-bar for the vertical displacement at the site, Kurikoma2, is an order-of-magnitude greater than the others. The calculated GPS displacements are based on our two-segment fault model with distributed slip as shown in Figure 11. Plan view of the fault model in Figure 11 is also indicated with black line with thick ones representing the top edge. The star and triangle indicate the epicenter and Mt. Kurikoma, respectively. Aftershocks are also shown with dots for comparison.

Figure 9: (a) Calculated InSAR data for the ascending track 402 from the fault model in Figure 11, and (b) misfit residuals from the observed one in Figure 2c. (c) Calculated InSAR data for the descending track 57 from the fault model in Figure 11, and (d) misfit residuals from the observed one in Figure 2d. Plan view of the fault model in Figure 11 is also indicated with black line with thick ones representing the top edge.

Figure 10: (a) Calculated range offset data for the ascending track 402 from the fault model in Figure 12, and (b) misfit residuals from the observed one in Figure 2e. (c) Calculated range offset data for the descending track 57 from the fault model in Figure 11, and (d) misfit residuals from the observed one in Figure 2f. (e) Calculated azimuth offset data for the descending track 57 from the fault model in Figure 11, and (f) misfit residuals from the observed one in Figure 2h.

Figure 11: Geometry and slip distribution of the east-dipping (F1) and west-dipping (F2) segment model inferred from GPS and SAR data. (a) Dip slip component for F1, (b) Dip slip component for F2, (c) Left-lateral slip component for F1, (d) Left-lateral slip component for F2. Note the difference in the scale of color bars. (e and f) 3D perspective of the fault geometry viewed from (e) SWS and (f) ENE.

Figure 12: Error estimates for the inferred slip distributions in Figures 11a-11d.

Figure 13: (a) Observed 3D displacements derived from the SAR data by Ando and Okuyama

(2010). Vectors represent horizontal displacements, colors represent vertical displacements. (b) Calculated 3D displacements, based on the source model in Figure 12. (c) Misfit residuals from the observed 3D displacements. The star and triangle indicate the epicenter and Mt. Kurikoma, respectively. The black dot indicates the GPS station, Kurikoma2.

Figure 14: Bouguer gravity anomaly and the location of the two-segment fault model. The black and red lines indicate top edge of the west-, and east-dipping fault model, respectively. KRK stands for Mt.Kurikoma. The star indicates the epicenter.

Figure 1
Click here to download high resolution image

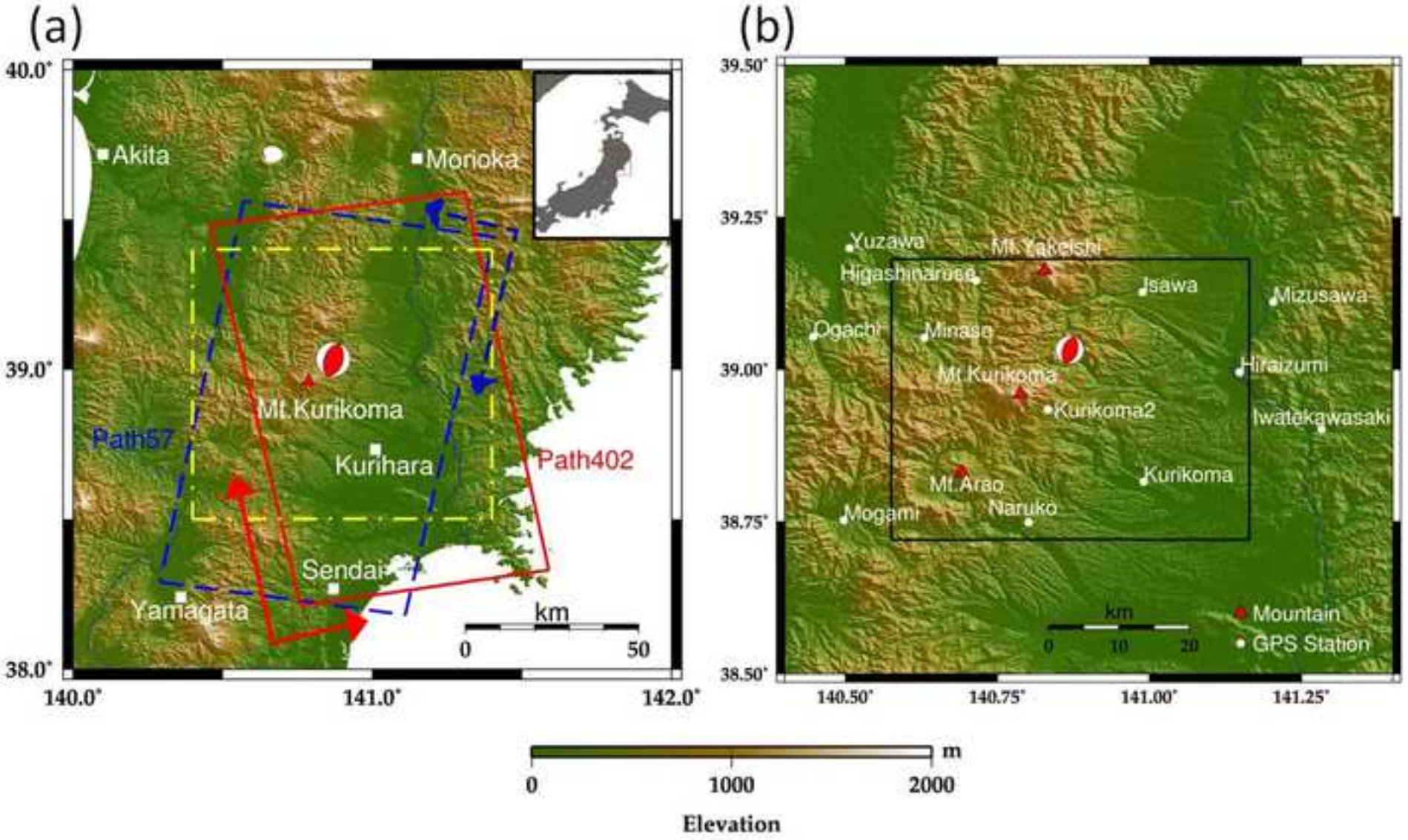

Figure 2
Click here to download high resolution image

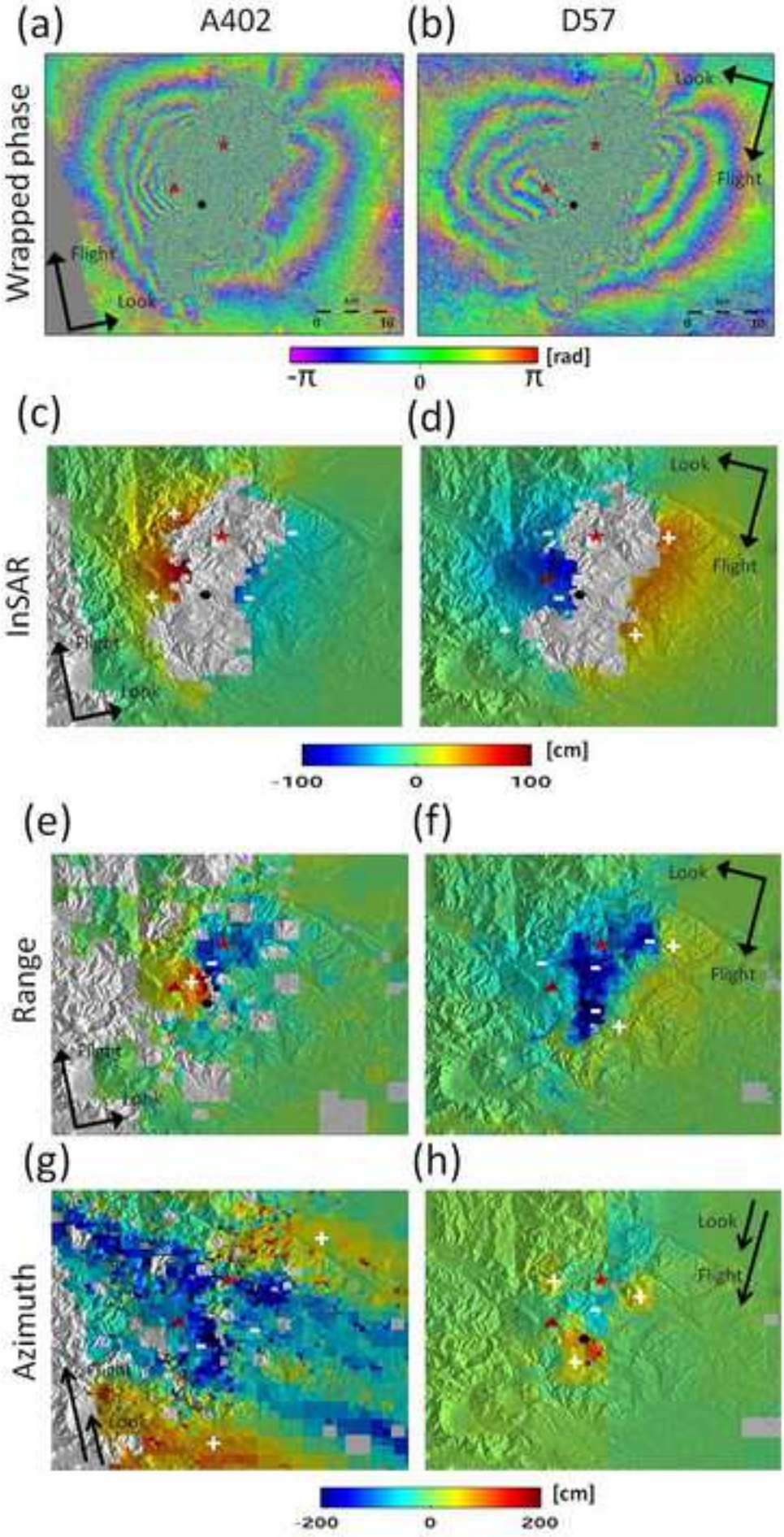

Figure 3
Click here to download high resolution image

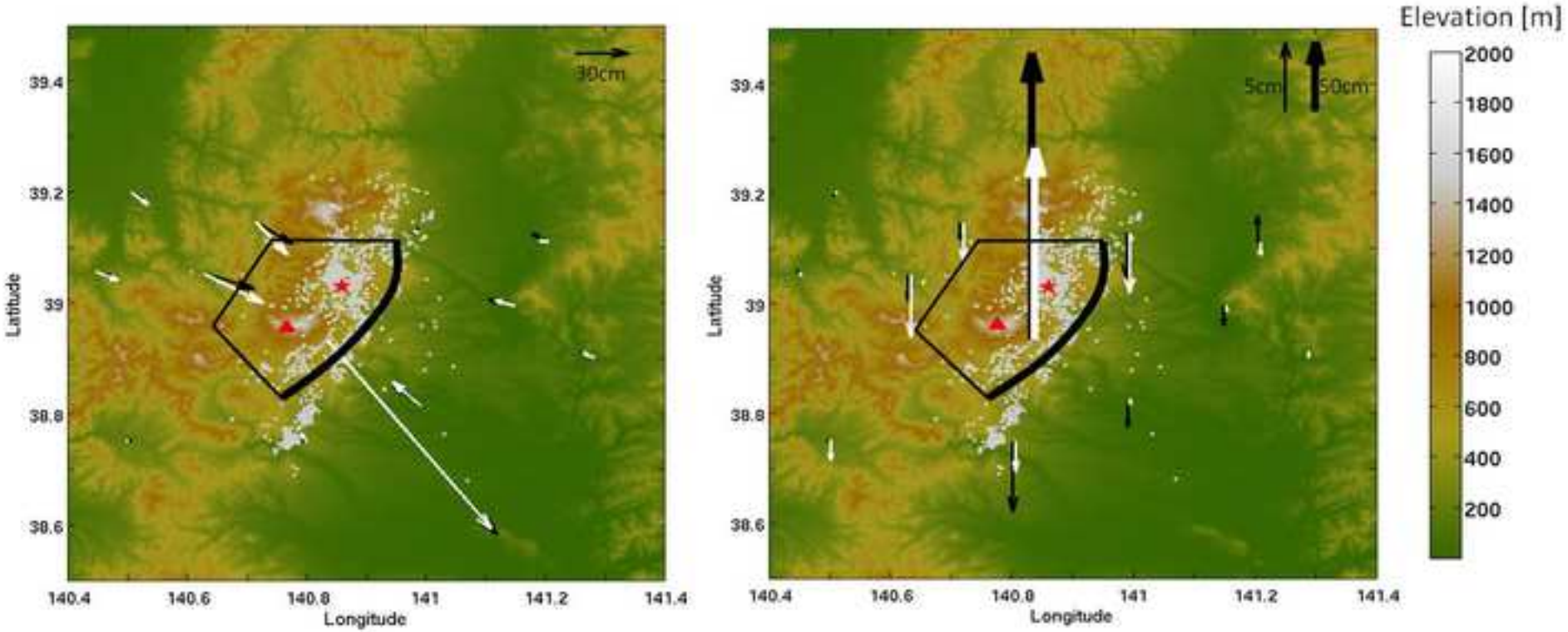

Figure 4
Click here to download high resolution image

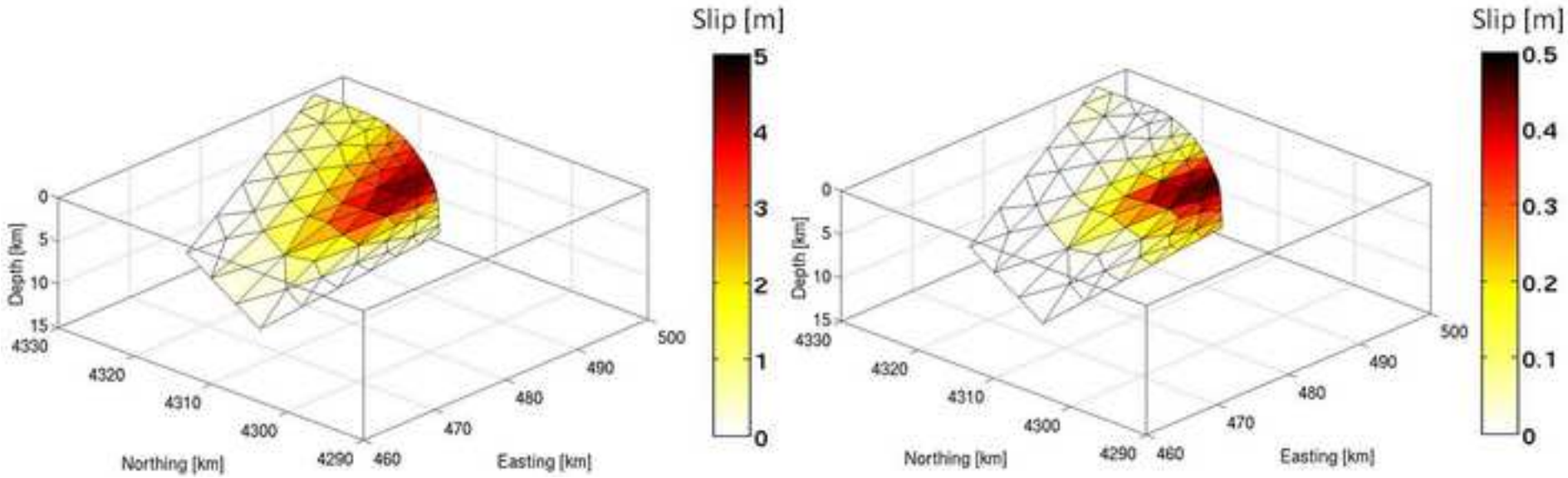

Figure 5
Click here to download high resolution image

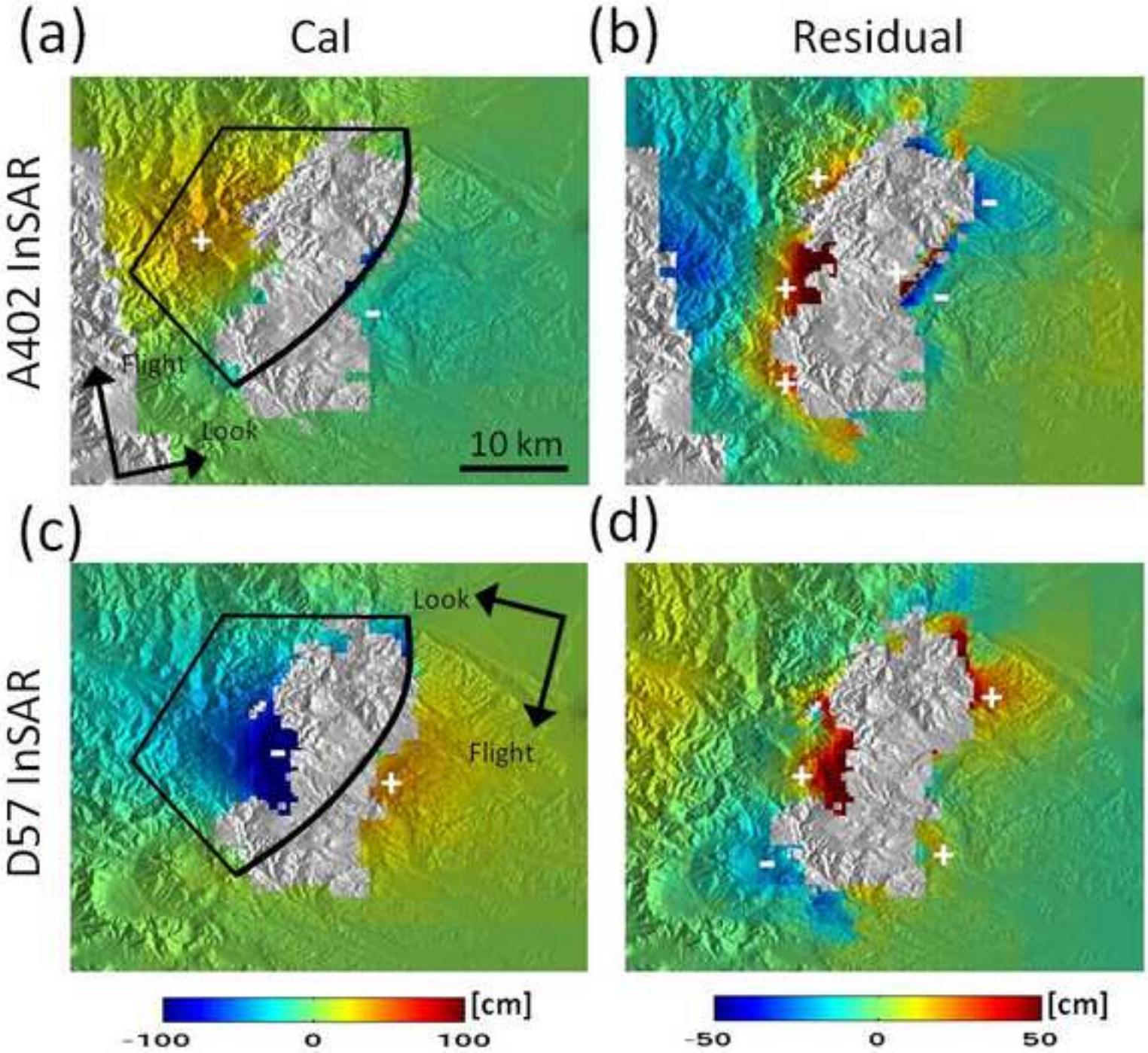

Figure 6
Click here to download high resolution image

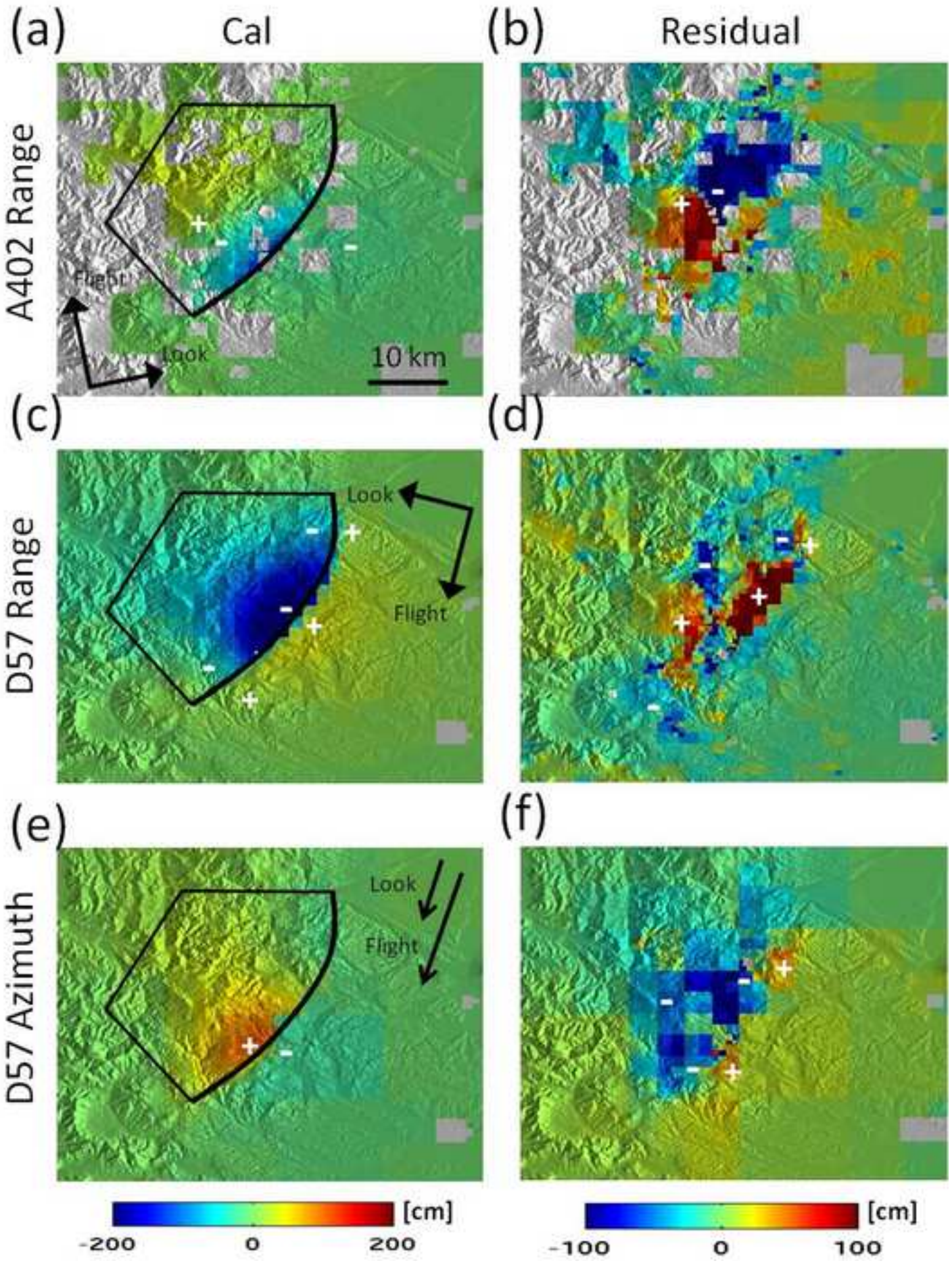

Figure 7
Click here to download high resolution image

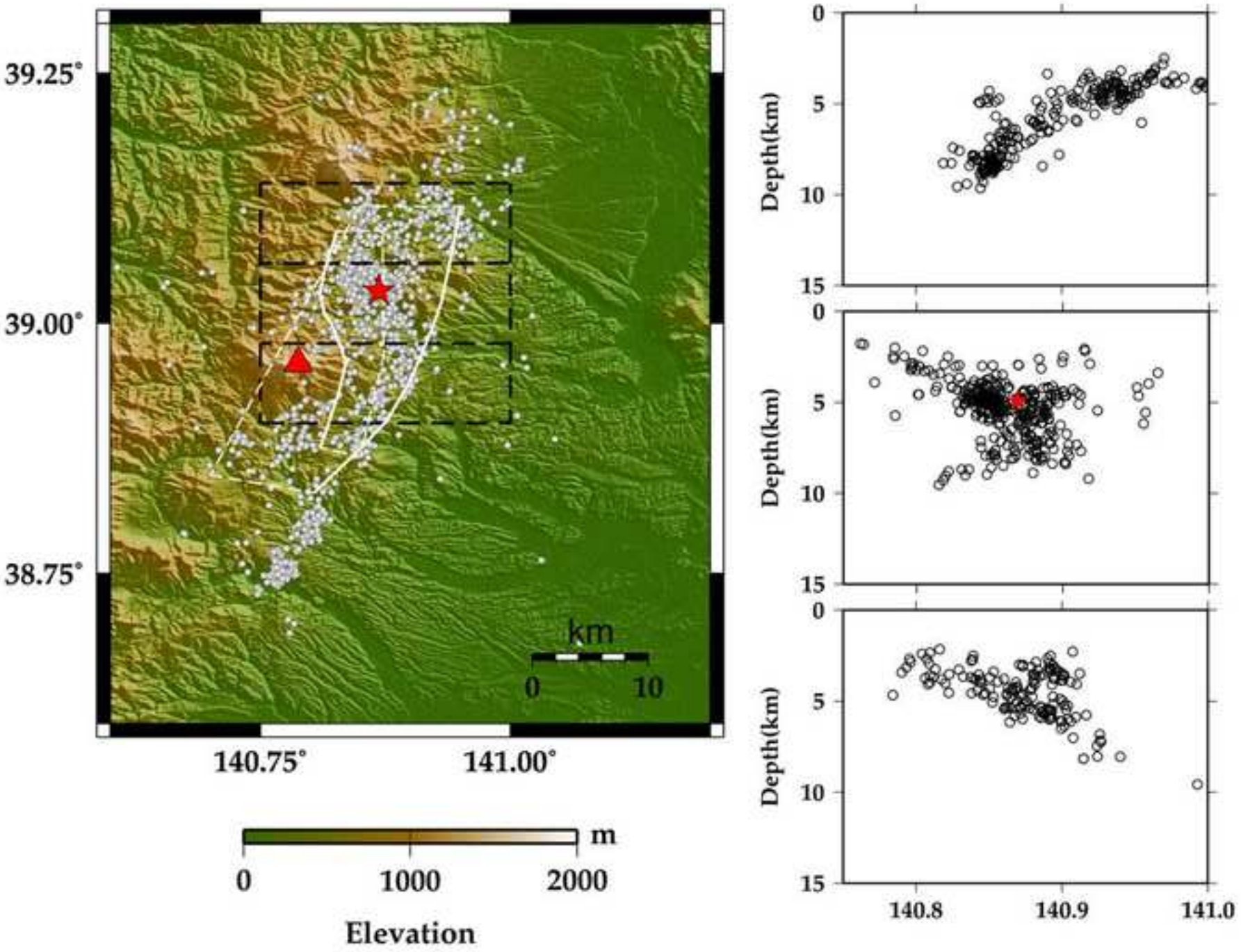

Figure 8
Click here to download high resolution image

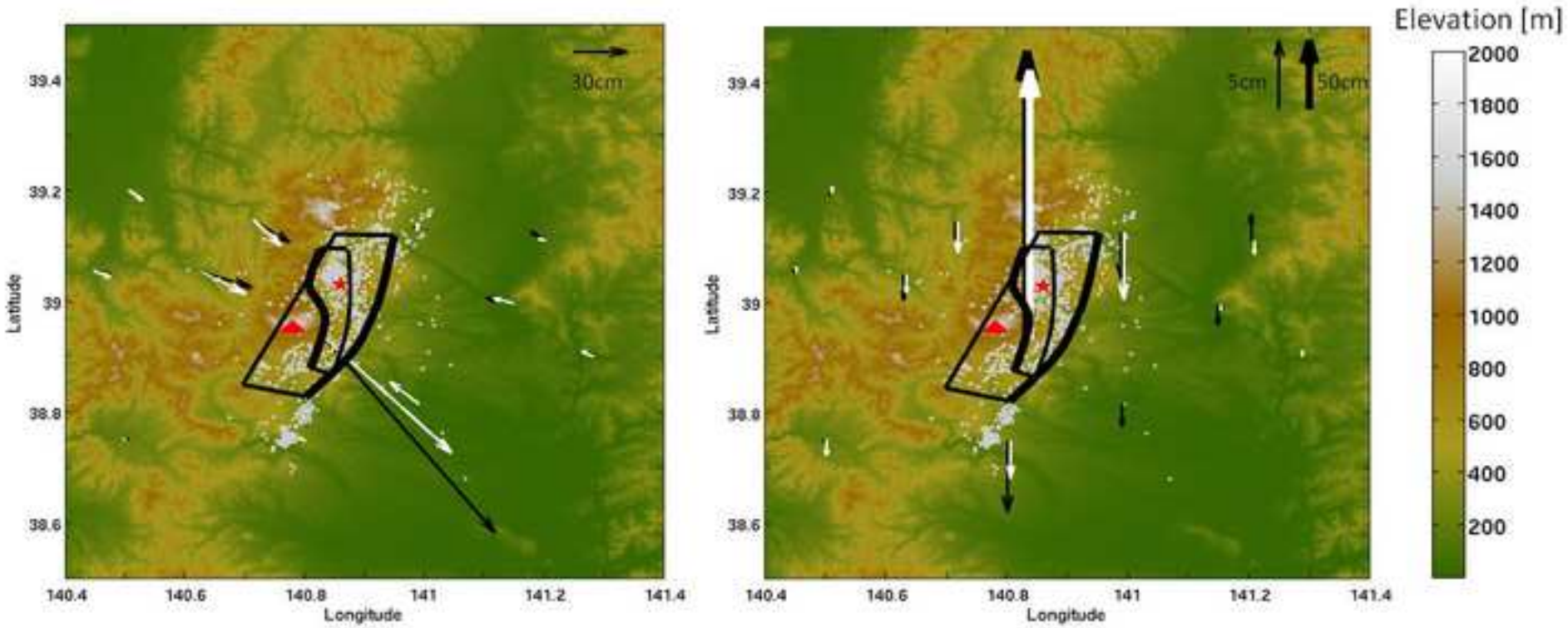

Figure 9
Click here to download high resolution image

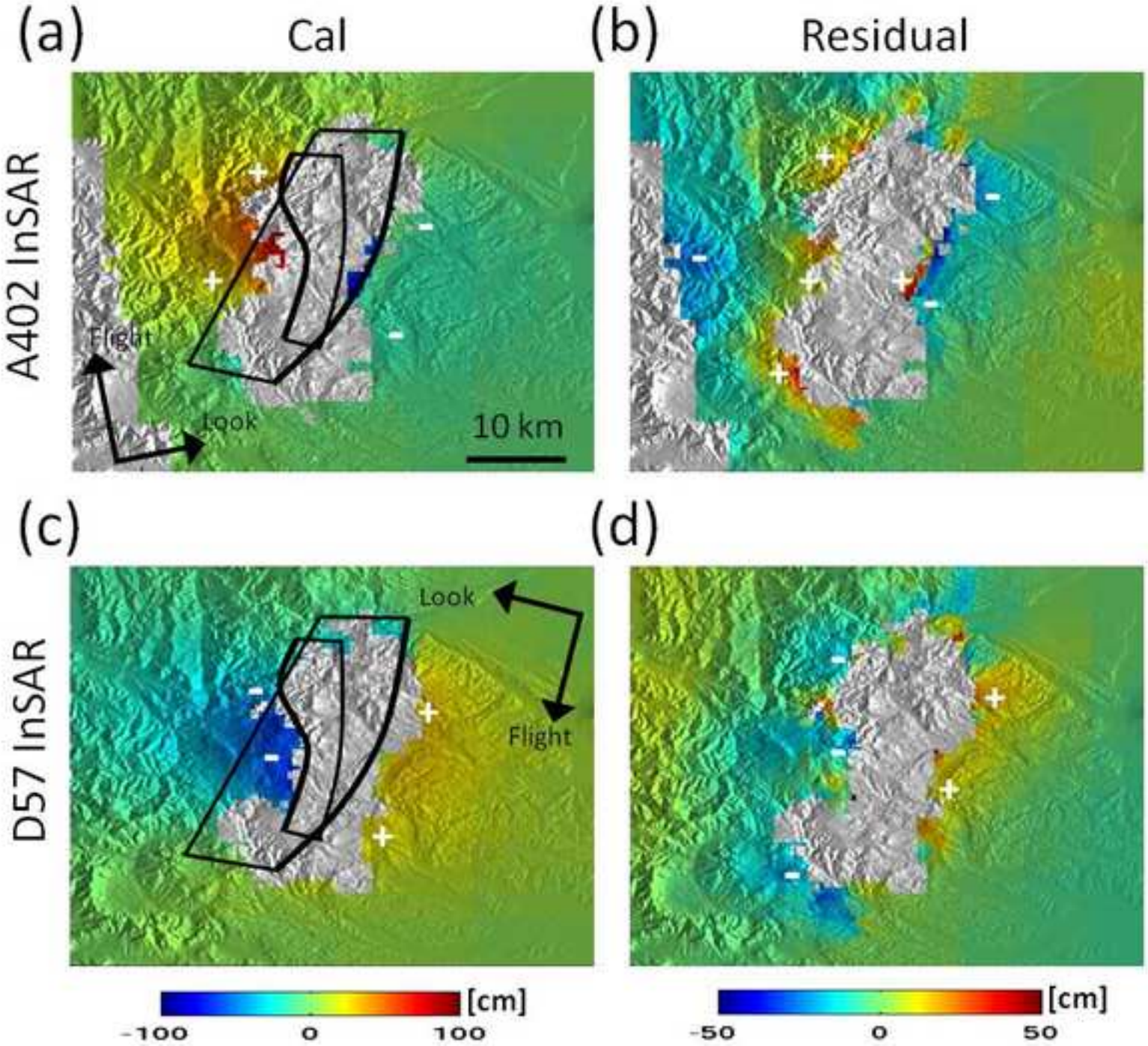

Figure 10
Click here to download high resolution image

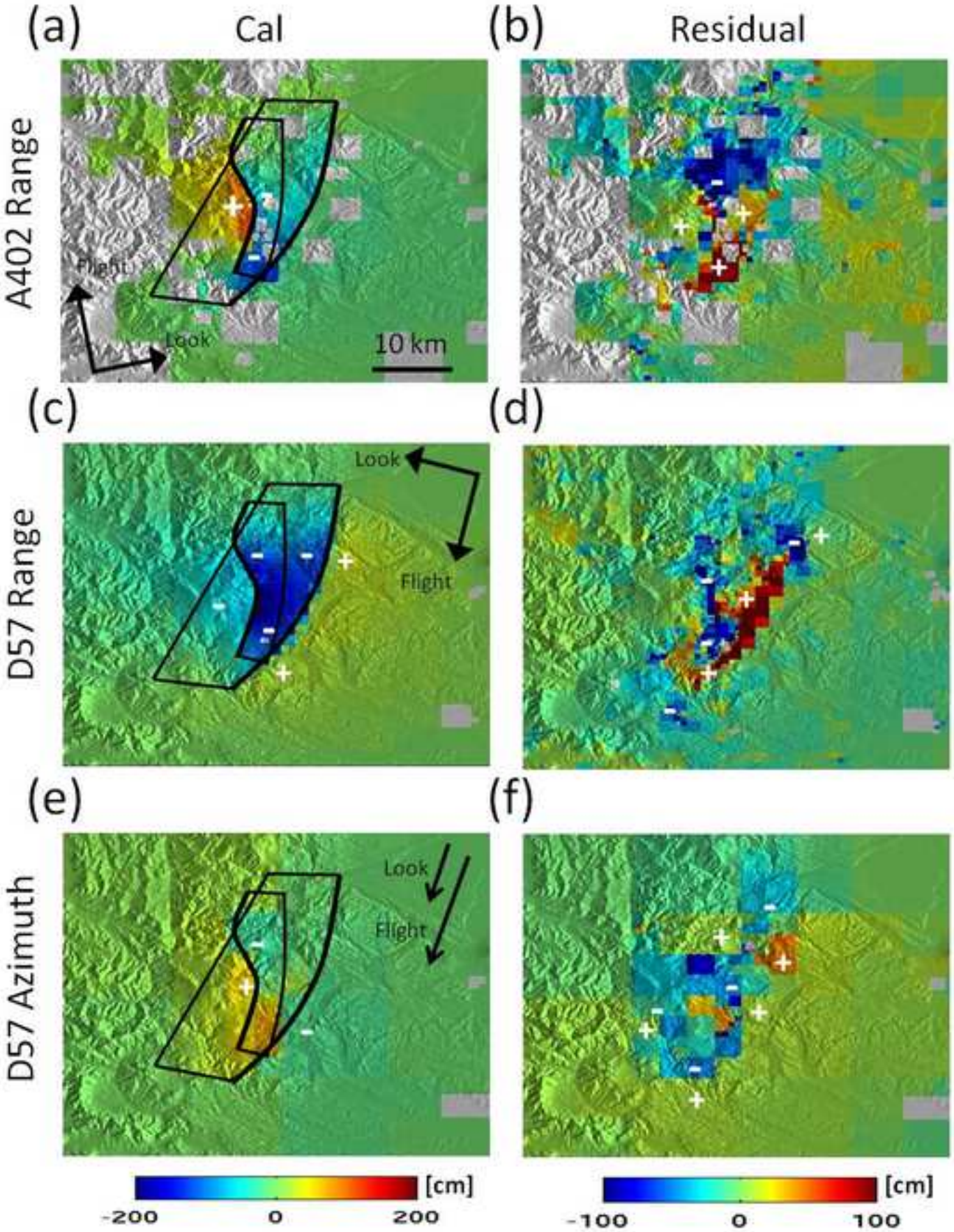

Figure 11
Click here to download high resolution image

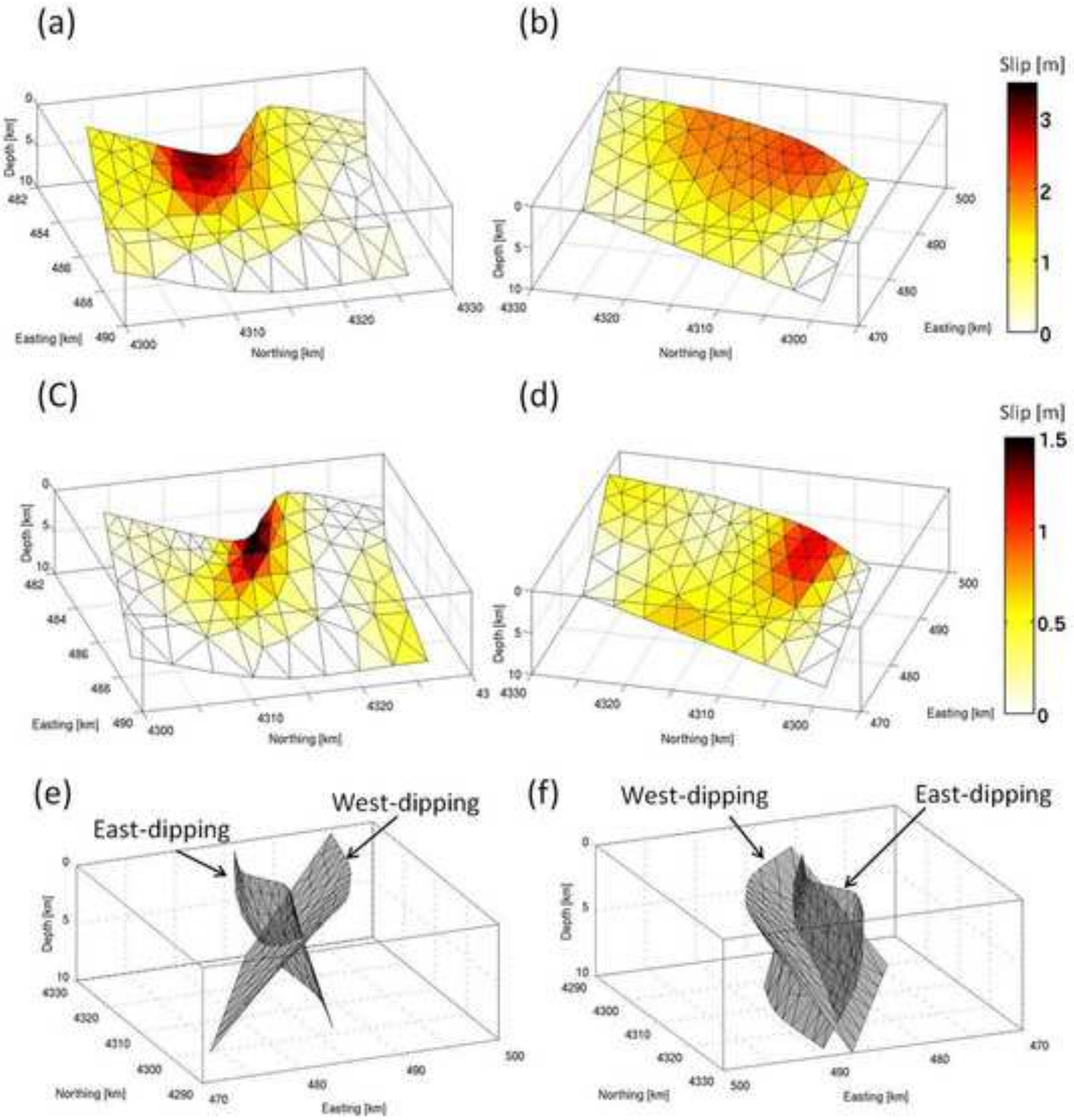

Figure 12
Click here to download high resolution image

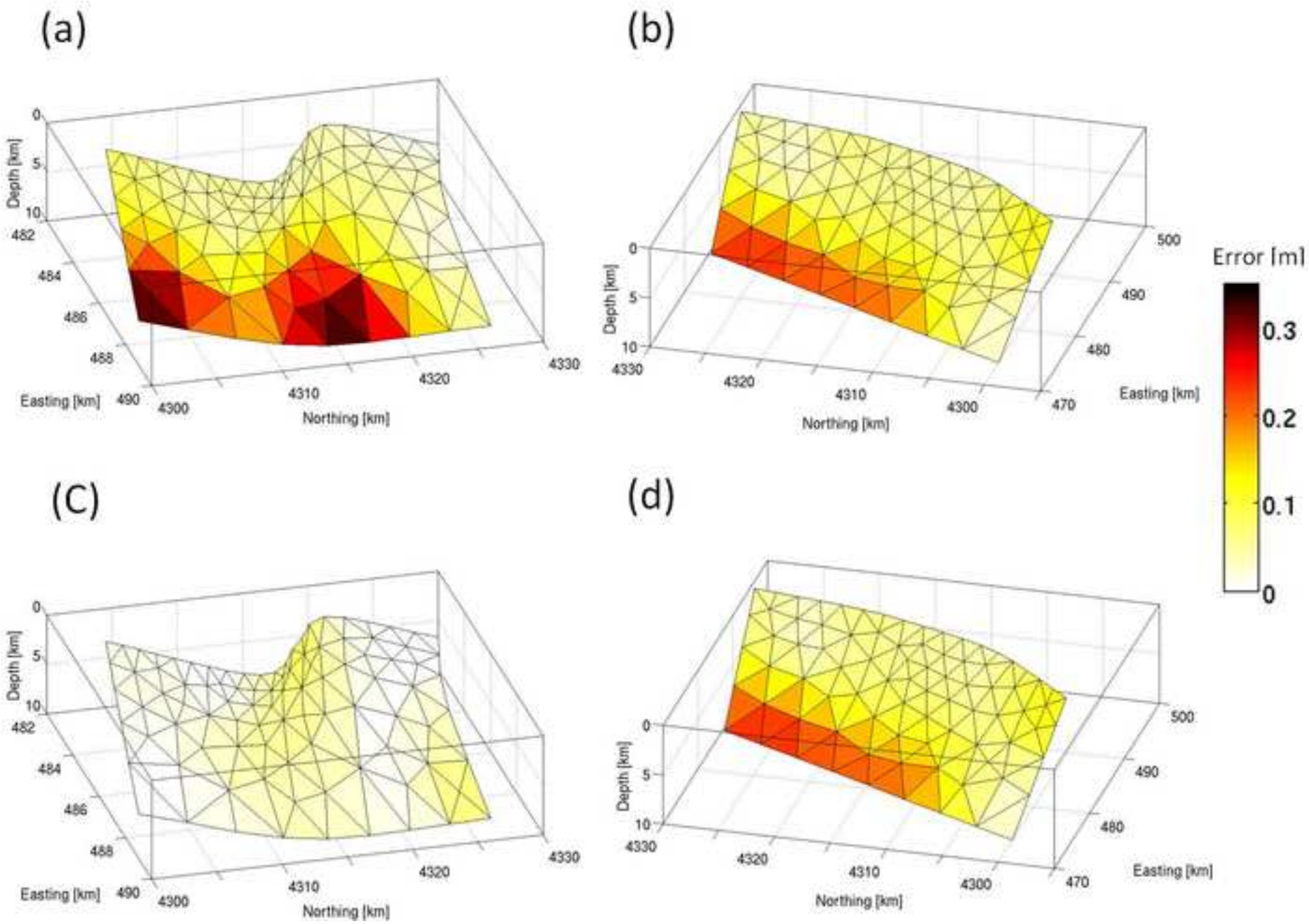

Figure 13
Click here to download high resolution image

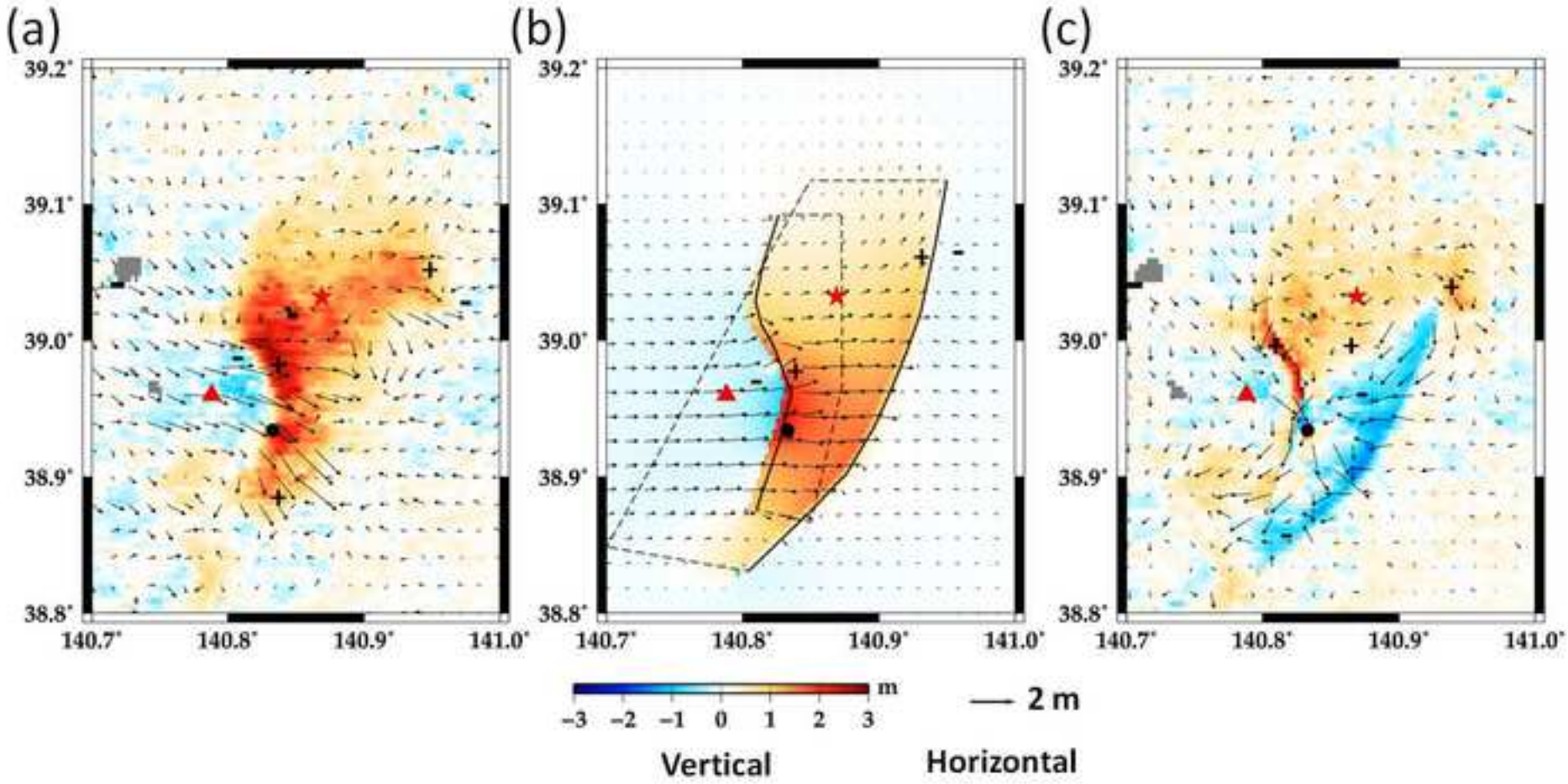

Figure 14
Click here to download Figure: AbeRevMod230.pdf